High-temperature, continuous-wave operation of terahertz quantum-cascade lasers with metal-metal waveguides and third-order distributed feedback

M. Wienold*, B. Röben, L. Schrottke, R. Sharma, A. Tahraoui, K. Biermann, and H. T. Grahn

Paul-Drude-Institut für Festkörperelektronik, Hausvogteiplatz 5–7, 10117 Berlin, Germany

* *wienold@pdi-berlin.de*

Abstract: Currently, different competing waveguide and resonator concepts exist for terahertz quantum-cascade lasers (THz QCLs). We examine the continuous-wave (cw) performance of THz QCLs with single-plasmon (SP) and metal-metal (MM) waveguides fabricated from the same wafer. While SP QCLs are superior in terms of output power, the maximum operating temperature for MM QCLs is typically much higher. For SP QCLs, we observed cw operation up to 73 K as compared to 129 K for narrow ($\leq 15\ \mu$m) MM QCLs. In the latter case, single-mode operation and a narrow beam profile were achieved by applying third-order distributed-feedback gratings and contact pads which are optically insulated from the intended resonators. We present a quantitative analytic model for the beam profile, which is based on experimentally accessible parameters.

OCIS codes: (140.5965) Semiconductor lasers, quantum cascade; (140.3490) Lasers: Distributed-feedback; (140.3070) Infrared and far-infrared lasers.

References and links

1. B. S. Williams, "Terahertz quantum-cascade lasers," Nat. Photonics **1**, 517–525 (2007).
2. S. Kumar, "Recent progress in terahertz quantum cascade lasers," IEEE J. Sel. Topics Quantum Electron. **17**, 38–47 (2011).
3. B. S. Williams, S. Kumar, Q. Hu and J. L. Reno, "High-power terahertz quantum-cascade lasers," Electron. Lett. **42**, 89–90 (2006).
4. M. Brandstetter, C. Deutsch, M. Krall, H. Detz, D. C. MacFarland, T. Zederbauer, A. M. Andrews, W. Schrenk, G. Strasser, and K. Unterrainer, "High power terahertz quantum cascade lasers with symmetric wafer bonded active regions," Appl. Phys. Lett. **103**, 171113 (2013).
5. B. S. Williams, S. Kumar, H. Callebaut, Q. Hu, and J. L. Reno, "Terahertz quantum-cascade laser at $\lambda \approx 100\ \mu$m using metal waveguide for mode confinement," Appl. Phys. Lett. **83**, 2124–2126 (2003).
6. B. S. Williams, S. Kumar, Q. Hu, and J. L. Reno, "Operation of terahertz quantum-cascade lasers at 164 K in pulsed mode and at 117 K in continuous-wave mode," Opt. Express **13**, 3331–3339 (2005).
7. S. Fathololoumi, E. Dupont, C. W. I. Chan, Z. R. Wasilewski, S. R. Laframboise, D. Ban, A. Mátyás, C. Jirauschek, Q. Hu, and H. C. Liu, "Terahertz quantum cascade lasers operating up to $\sim$ 200 K with optimized oscillator strength and improved injection tunneling," Opt. Express **20**, 3866–3876 (2012).
8. L. Mahler, and A. Tredicucci, "Photonic engineering of surface-emitting terahertz quantum cascade lasers," Laser & Photon. Rev. **5**, 647–658 (2011).
9. M. I. Amanti, G. Scalari, F. Castellano, M. Beck, and J. Faist, "Low divergence terahertz photonic-wire laser," Opt. Express **18**, 6390–6395 (2010).
10. G. Xu, R. Colombelli, S. P. Khanna, A. Belarouci, X. Letartre, L. Li, E. H. Linfield, A. G. Davies, H. E. Beere, and D. A. Ritchie, "Efficient power extraction in surface-emitting semiconductor lasers using graded photonic heterostructures," Nat. Commun. **3**, 952 (2012).

#199359 - $15.00 USD Received 14 Oct 2013; revised 18 Dec 2013; accepted 18 Jan 2014; published 5 Feb 2014

11. M. I. Amanti, M. Fischer, G. Scalari, M. Beck, and J. Faist, "Low-divergence single-mode terahertz quantum cascade laser," Nat. Photonics **3**, 586–590 (2009).
12. S. Kohen, B. S. Williams, and Q. Hu, "Electromagnetic modeling of terahertz quantum cascade laser waveguides and resonators," J. Appl. Phys. **97**, 053106 (2005).
13. G. Scalari, N. Hoyler, M. Giovannini, and J. Faist, "Terahertz bound-to-continuum quantum-cascade lasers based on optical-phonon scattering extraction," Appl. Phys. Lett. **86**, 181101 (2005).
14. M. S. Vitiello, G. Scamarcio, V. Spagnolo, J. Alton, S. Barbieri, C. Worrall, H. E. Beere, D. A. Ritchie, and C. Sirtori, "Thermal properties of THz quantum cascade lasers based on different optical waveguide configurations," Appl. Phys. Lett. **89**, 021111 (2006).
15. M. Cui, J. N. Hovenier, Y. Ren, N. Vercruyssen, J. R. Gao, T. Y. Kao, Q. Hu, and J. L. Reno, "Beam and phase distributions of a terahertz quantum cascade wire laser," Appl. Phys. Lett. **102**, 111113 (2013).
16. T.-Y. Kao, Q. Hu, and J. L. Reno, "Perfectly phase-matched third-order distributed feedback terahertz quantum-cascade lasers," Opt. Lett. **37**, 2070–2072 (2012).
17. E. E. Orlova, J. N. Hovenier, T. O. Klaassen, I. Kašalynas, A. J. L. Adam, J. R. Gao, T. M. Klapwijk, B. S. Williams, S. Kumar, Q. Hu, and J. L. Reno, "Antenna model for wire lasers," Phys. Rev. Lett. **96**, 173904 (2006).
18. W. L. Stutzman, and G. A. Thiele, *Antenna theory and design* (Wiley, 2009).
19. J. L. Kloosterman, D. J. Hayton, Y. Ren, T. Y. Kao, J. N. Hovenier, J. R. Gao, T. M. Klapwijk, Q. Hu, C. K. Walker, and J. L. Reno, "Hot electron bolometer heterodyne receiver with a 4.7-THz quantum cascade laser as a local oscillator," Appl. Phys. Lett. **102**, 011123 (2013).
20. M. Wienold, L. Schrottke, M. Giehler, R. Hey, W. Anders, and H. T. Grahn, "Low-voltage terahertz quantum-cascade lasers based on LO-phonon-assisted interminiband transitions," Electron. Lett. **45**, 1030–1031 (2009).
21. A. Benz, G. Fasching, A. M. Andrews, M. Martl, K. Unterrainer, T. Roch, W. Schrenk, S. Golka, and G. Strasser, "Influence of doping on the performance of terahertz quantum-cascade lasers," Appl. Phys. Lett. **90**, 101107 (2007).
22. M. I. Amanti, G. Scalari, R. Terazzi, M. Fischer, M. Beck, J. Faist, A. Rudra, P. Gallo and E. Kapon, "Bound-to-continuum terahertz quantum cascade laser with a single-quantum-well phonon extraction/injection stage," N. J. Phys. **11**, 125022 (2009).
23. M. Wienold, A. Tahraoui, L. Schrottke, R. Sharma, X. Lü, K. Biermann, R. Hey, and H. T. Grahn, "Lateral distributed-feedback gratings for single-mode, high-power terahertz quantum-cascade lasers," Opt. Express **20**, 11207–11217 (2012).
24. K. Biermann, E. A. Cerda-Méndez, M. Höricke, P. V. Santos, and R. Hey, "Controlled growth of exciton-polariton microcavities using in situ spectral reflectivity measurements," J. Cryst. Growth **323**, 56-59 (2011).
25. J. Faist, "Wallplug efficiency of quantum cascade lasers: Critical parameters and fundamental limits," Appl. Phys. Lett. **90**, 253512 (2007).

1. Introduction

By today, terahertz quantum-cascade lasers (THz QCLs) are established sources for various applications in the field of spectroscopy and imaging (for reviews see [1,2]). One target for the development of these sources is continuous-wave (cw) operation above 80 K, which allows for cooling with liquid nitrogen. Most of the reported scientific applications in the last decade rely on THz QCLs based on single-plasmon (SP) waveguides, which operate typically only up to 70 K. For SP waveguides, the optical mode is confined by a top-metal layer and a highly doped contact layer underneath the active region. SP QCLs are relatively easy to fabricate, exhibit high levels of output power, and a beam profile, which is suitable for focusing optics. While SP waveguides are well suited for many applications and superior in terms of output power [3,4], all records in terms of operating temperatures are held by THz QCLs based on metal-metal (MM) waveguides, for which the active region is sandwiched between two metal layers [5–7]. However, due to the strong sub-wavelength confinement, edge emitting MM QCLs suffer from a poor beam profile. To overcome this limitation, many efforts have been put into the development of surface emitting MM QCLs [8]. However, a convincing combination of high output power, cw operation, and a good beam profile have only been demonstrated recently [9,10]. Amanti et al. [9,11] have shown that most drawbacks of edge emitting and surface emitting MM QCLs can be avoided by applying a distributed-feedback (DFB) grating of third order (3ODFB). 3ODFB gratings have the inherent advantage to allow for a collimation of the beam in two orthogonal directions, even for sub-wavelength ridge widths. In the ideal case, they provide a combination

#199359 - $15.00 USD Received 14 Oct 2013; revised 18 Dec 2013; accepted 18 Jan 2014; published 5 Feb 2014

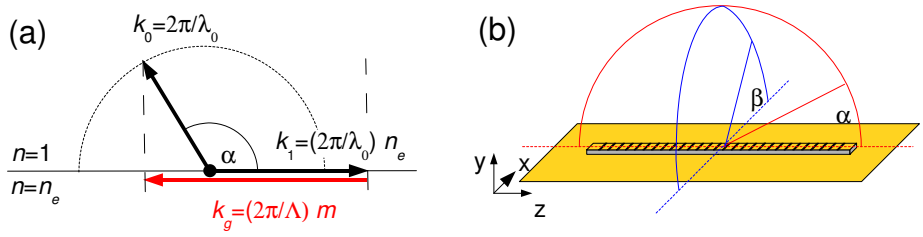

Fig. 1. (a) Surface emission in k-space for a linear grating emitter (n: refractive index). (b) Idealized linear surface emitter and coordinate system as used in this paper.

of an application-friendly beam profile, single-mode operation, and small cw driving powers. However, many aspects of this type of resonator are still lacking a detailed understanding. In this work, we present for the same wafer a comparison of the performance of SP QCLs, MM QCLs with a Fabry-Pérot (FP) resonator, and MM QCLs with a 3ODFB resonator. In the case of MM QCLs, we focus on MM wire QCLs, i.e. QCLs for which the ridge width is much smaller than the free-space wavelength. In contrast to MM wire QCLs, typical SP QCLs are more or less classical edge emitters, which perform best if the ridge width is of the same dimension or even larger than the free space wavelength [3, 4, 12]. Hence, MM wire QCLs and SP QCLs are practically two different classes of devices, which do not allow for a meaningful systematic comparison in terms of device parameters such as the ridge width. For studies on SP and MM waveguides in general, we refer the reader to the literature [12–14].

2. Surface emission by linear distributed-feedback gratings

In the pioneering work [11], it was already noted that the beam profile of 3ODFB QCLs shows similarities with that of antenna arrays used for radio- and micro-wave sources. In this section, we will show, how the well-established theory of antenna arrays can be extended to yield not only a phenomenological model of the far field [9, 15], but a quantitative analytic relation between the longitudinal resonator modes and the emission profile. There has been a discussion in the literature about the role of the effective refractive index for the emission characteristics of 3ODFB QCLs [11, 15, 16] with the consensus that the ideal case would be a value of 3. The grating acts then as an end-fire antenna array with emission cones in the ridge direction. However, the concept of an effective index has to be used with caution, since the effective index is usually defined as the eigenvalue of the transverse modes of an (infinitely long) waveguide. While waveguides exhibit a continuous spectrum for the guided modes, the mode spectrum of resonators is discrete due to the boundary conditions. We will develop an antenna model in which the beam characteristics is fully described by geometrical parameters, the emission wavelength, and an integer number, which corresponds to the number of intensity maxima inside the resonator.

We start with some basic considerations about surface emission mediated by linear distributed-feedback gratings. For a DFB grating of order M and period Λ, the vacuum Bragg wavelength is $\lambda_B^{(M)} = 2n_e\Lambda/M$, where n_e denotes the effective refractive index of the waveguide. The situation in k-space for surface emission from a linear grating emitter is illustrated in Fig. 1(a). Three k-vectors are involved: one for the radiated wave with propagation constant

#199359 - $15.00 USD Received 14 Oct 2013; revised 18 Dec 2013; accepted 18 Jan 2014; published 5 Feb 2014

$k_0 = 2\pi/\lambda_0$, one for the incident waveguide mode with propagation constant $k_1 = 2\pi n_e/\lambda_0$, and one grating vector with magnitude $k_g = m2\pi/\Lambda$, where λ_0 denotes the free-space wavelength and m the diffraction order. Due to the electromagnetic boundary conditions, the propagation vector parallel to the surface must be conserved. This results in the following relation for the emission angle α:

$$\cos(\alpha) = n_e - \frac{\lambda_0}{\Lambda} m \,, \;\; (|m| \geq 1). \tag{1}$$

In general, λ_0 differs from $\lambda_B^{(M)}$. Therefore, we will treat λ_0 and Λ as independent here. For surface emission, the absolute value of the right-hand side of Eq. (1) must be equal or smaller than 1. For $n_e > 3$, this condition results in a radiation gap around $\lambda_B^{(3)}$, for which no light is emitted. The radiation gap, spanned by the second and first diffraction orders, occurs between

$$\frac{n_e + 1}{2} \leq \frac{\lambda_0}{\Lambda} \leq n_e - 1 \,. \tag{2}$$

There has been some debate, whether the effective index n_e has to be smaller than 3 for surface emission from an arbitrarily long third-order grating emitter. However, for an index grating, the condition for surface emission is always fulfilled, if the width of the DFB stop band (centered around the Bragg frequency) exceeds the width of the radiation gap by more than $4/3$ (the value is not 1, since the third-order radiation gap is not centered around the Bragg frequency). Note that for third-order gratings surface emission is caused by the first and second diffraction orders ($m = \pm 1, \pm 2$), while the distributed feedback of the grating is caused by the third diffraction order ($m = \pm 3$). The feedback due to facet reflections corresponds to the zeroth diffraction order.

In order to describe the beam profile of MM wire QCLs, Orlova et al. [17] proposed an antenna model for long lasers with sub-wavelength apertures. Later, the theory of antenna arrays was applied to describe the emission profile of 3ODFB QCLs [11]. Within this approach, the grating slits are considered as an array of individual antennas, and the beam profile is given by the product of an array factor and the emission profile of the individual antennas. For isotropic emitters, the array factor itself resembles the beam profile. A typical configuration is a MM wire QCL on top of the substrate plane, which is covered with a highly reflective Au layer [cf. Fig. 1(b)]. To account for reflections at the substrate plane, a mirror term can be introduced. Using the coordinate definitions of Fig. 1(b), the array factor for N emitters at positions $\mathbf{r_j}$ in a plane $y = h/2$ above the surface can be written as

$$A(\mathbf{k_0}) = \sum_{j=1}^{N} \left\{ a_j \exp(i\mathbf{r_j} \cdot \mathbf{k_0}) - a_j \exp\left(i[\mathbf{r_j} \cdot \mathbf{k_0} - hk_y]\right) \right\} \,. \tag{3}$$

Here, a_j denote the emitter amplitudes, k_y the component of $\mathbf{k_0}$ which is perpendicular to the surface plane, and h the distance between the grating surface and the image plane, which is twice the height of the waveguide ridge. It is instructive to consider the transition toward a dense spacing of emitters, for which the sum can be replaced by an integral over an aperture area S_a. With the approximation $\exp(-ihk_y) \approx 1 - ihk_y$, which is justified for $k_y h \ll 1$, Eq. (3) becomes

$$A(\mathbf{k_0}) = \frac{ihk_y}{S_a} \int_{S_a} a(\mathbf{r}) \exp(i\mathbf{r} \cdot \mathbf{k_0}) dS \,. \tag{4}$$

This resembles (except for a constant prefactor) the common expression for the far field as obtained by the Fourier transform of an aperture near field [18]. The amplitude $a(\mathbf{r})$ and the array factor $A(\mathbf{k_0})$ can be identified with the near-field and far-field components of the electromagnetic field, respectively. Note that Eq. (4) is well justified only in the case of outgoing waves

#199359 - $15.00 USD Received 14 Oct 2013; revised 18 Dec 2013; accepted 18 Jan 2014; published 5 Feb 2014

polarized in the plane of the considered near-field aperture. Strictly, it requires a decomposition of the near field into outward and inward directed components, which makes Eq. (4) in general difficult to be used with the result of finite-element near-field simulations.

For the antenna model, the emitter amplitudes a_j are required. As a first approximation, these can be set to unity or to follow an assumed envelope [15]. Here, we follow a slightly different approach based on an analytic expression for the emitter amplitudes a_j, which is consistent with the assumption of a constant intensity envelope inside the resonator. In general, the beam profile of a grating emitter is not necessarily symmetric. However, we restrict ourselves to grating emitters consisting of a number of N emitters, which are equally spaced by Λ on a resonator with length $(N-1)\Lambda$. Therefore, the resonator is symmetric with respect to its center in the z-direction (which we set $z=0$), and we write for the amplitudes a_j:

$$a_j = a_+(z_j)e^{i\phi_j} + s\, a_-(z_j)e^{-i\phi_j}\,, \tag{5}$$

where $a_\pm$ denote real functions fulfilling $a_+(z) = a_-(-z)$. s denotes the symmetry factor, which is $+1$ (-1) for symmetric (antisymmetric) resonator modes corresponding to modes with an odd (even) number of intensity maxima. ϕ_j is the relative phase for each emitter given by

$$\phi_j = 2\pi\left(j - \frac{N+1}{2}\right)\frac{\Lambda}{\lambda_0}n_r\,. \tag{6}$$

Here, n_r denotes the effective refractive index for the resonator mode with longitudinal index r, where r equals the number of intensity maxima inside the resonator. How is n_r related to n_e? While n_e is defined for a waveguide (no grating, no facets), we define n_r for a resonator. In general, n_r is affected by the boundary conditions at the facets and the DFB grating. For a vanishing distributed feedback and an infinitely long cavity, n_r equals n_e.

We further restrict ourselves to the case of weak coupling and high facet reflectivity, for which the intensity envelope inside the resonator is more or less constant. We set $a_+ = a_- = 1$. Note that this neither implies that the field amplitudes a_j equal each other, nor that the total intensity in the near and far field remains constant for different grating parameters. The boundary conditions (zero field amplitude at the facets) are satisfied for

$$n_r = \frac{r\lambda_0}{2(N-1)\Lambda}\,. \tag{7}$$

Figures 2(a)–2(d) depict four calculated far-field intensity profiles $|A|^2$ according to Eq. (3) as a function of α and a dimensionless parameter $p = n_r\Lambda/\lambda_0$. In Figs. 2(a) and 2(b), the results are shown for $s = \pm 1$ and a value n_r smaller than 3, while Figs. 2(c) and 2(d) depict the situation for a value n_r larger than 3. The values for p, which fulfill exactly the boundary conditions according to Eq. (7), are marked by black horizontal lines. The cases $\lambda_0 = \lambda_B^{(M)}$ for second- ($M=2$) and third-order ($M=3$) gratings correspond to $p = 1$ and $3/2$, respectively. They are characterized by emission perpendicular to the surface ($M=2$) or emission in a small angle with the ridge axis ($M=3$). The transitions between the grating orders with respect to their emission characteristics are smooth. For $n_r > 3$, a radiation gap is observed around $p = 3/2$ according to Eq. (2) [cf. Figs. 2(c) and 2(d)]. No light is emitted below a cut-off value $p < n_r/(n_r+1)$. There exist no parameters, for which emission at $\alpha = 0^\circ$ is obtained, which is due to the presence of an infinite metal plane underneath the resonator. In such a configuration, emission in the ridge direction, as for classical edge-emitting ridge lasers, cannot be obtained irrespective of the particular grating parameters. For $p \approx 1$, symmetric modes ($s=1$) emit mainly in a single lobe around $\alpha = 90^\circ$, while antisymmetric modes ($s=-1$) exhibit a pronounced double lobe

#199359 - $15.00 USD Received 14 Oct 2013; revised 18 Dec 2013; accepted 18 Jan 2014; published 5 Feb 2014

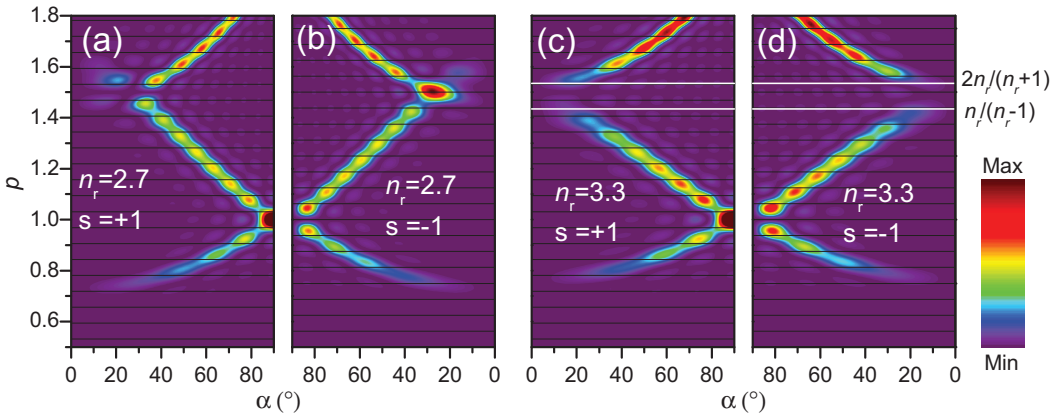

Fig. 2. Calculated far-field intensity as a function of α ($\beta = 90°$) and the dimensionless parameter $p = n_r\Lambda/\lambda_0$ according to Eq. (3) for a linear grating with 16 elements. (a) $n_r = 2.7$ and $s = +1$, (b) $n_r = 2.7$ and $s = -1$, (c) $n_r = 3.3$ and $s = +1$, (d) $n_r = 3.3$ and $s = -1$. For the black horizontal lines, the boundary conditions according to Eq. (7) are exactly fulfilled. For the definition of α and β, see Fig. 1(b).

with a zero at $\alpha = 90°$ as well as a vanishing intensity for $p = 1$. This nicely illustrates, why the longitudinal symmetry of the mode is the decisive parameter for THz QCLs with second-order DFB gratings. For third-order gratings, one finds that for an even number of emitters antisymmetric modes emit more efficiently around $p = 3/2$ than symmetric modes, while the situation is reversed for an odd number of emitters.

In the following, we focus on MM wire QCLs with a maximum ridge width of 15 μm. In order to calculate the resonator modes, we performed three-dimensional finite-element simulations for different resonator configurations using the software JCMsuite (JCMwave GmbH). In Fig. 3(a), the threshold gain is plotted for the various TM_{00} and TM_{01} modes of a FP resonator, while in Figs. 3(b) and 3(c) the threshold gain is plotted for two 3ODFB grating configurations. The configuration in Fig. 3(b) corresponds to the grating design of Amanti et al. [9], while in Fig. 3(c) a tapered configuration has been applied, which is closer to the experimental situation and similar to the grating design of Kloosterman et al. [19]. To obtain the threshold gain from the complex eigenvalues as determined by the software, each simulation has been performed for an empty cavity (zero gain in the active region) as well as for a cavity with a finite gain $g = g_0$ in the active region. The threshold gain for mode j is then determined by

$$g_{\mathrm{th}}^{(j)} = g_0 \frac{\omega_{i,g=0}^{(j)}}{\omega_{i,g=0}^{(j)} - \omega_{i,g=g_0}^{(j)}}\,, \tag{8}$$

where $\omega_i^{(j)}$ denotes the imaginary part of the obtained eigenvalue for mode j. Here, we assume that the gain acts as a small perturbation and does not change the mode confinement. In this limit, the results are independent of the particular value for g_0. The calculated threshold gain is due to intrinsic losses (α_i) and surface (or radiation) losses (α_r) according to $g_{\mathrm{th}} = -(\alpha_i + \alpha_r)$. In order to find the value of α_i, which corresponds to the displayed simulation results, we also performed three-dimensional simulations for a piece of the FP waveguide with periodic boundary conditions. From that, we obtained intrinsic losses of about 15 cm^{-1} for the TM_{00} mode in the displayed wavenumber range. Note that the numerical accuracy in Fig. 3 is limited

#199359 - $15.00 USD Received 14 Oct 2013; revised 18 Dec 2013; accepted 18 Jan 2014; published 5 Feb 2014

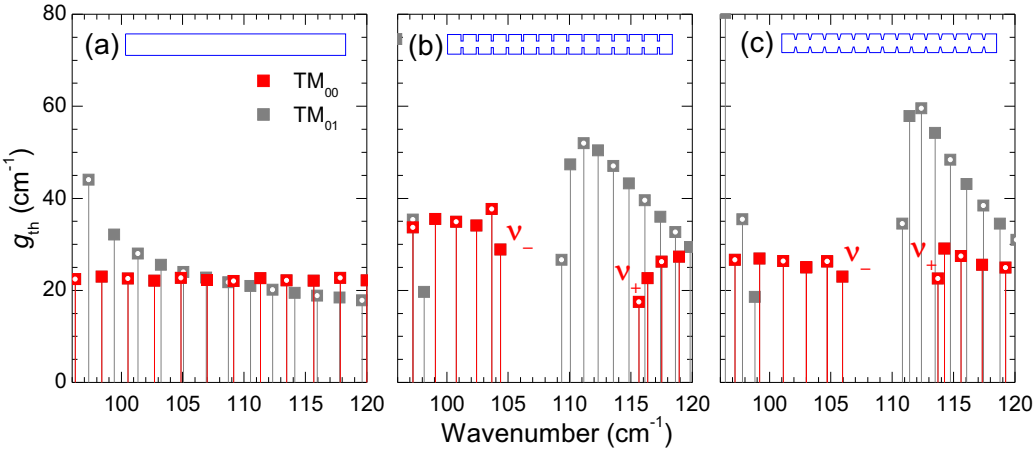

Fig. 3. Calculated threshold gain vs. wavenumber for a FP resonator and two 3ODFB resonators with 15 segments and $\Lambda = 45$ μm. (a) FP resonator with an area of 15×670 μm^2 and an active region thickness of 11 μm. (b) Square grating notches with 15% duty cycle and 15 μm (5 μm) width in the wide (narrow) section. (c) Tapered grating notches with 25% (7%) duty cycle and 15 μm (6 μm) width in the wide (narrow) region. Modes which are antisymmetric with respect to the longitudinal symmetry are labeled with white dots. A value of $g_0 = 30$ cm^{-1} was used for the calculations.

by the restrictions set by the computational requirements for three-dimensional calculations and by the uncertainties in the used material parameters [12]. Hence, the results are to be interpreted in a qualitative sense.

As expected for a FP resonator, the threshold gain remains rather constant for the different longitudinal modes with TM_{00} symmetry. The increase of g_{th} for TM_{01} modes (shown in grey) toward smaller wavenumbers is due to the low-frequency cut off for these modes around 90 cm^{-1}. In case of the 3ODFB grating, the distributed feedback results in the formation of stop bands. Since the effective index (n_e) differs for TM_{00} and TM_{01} modes, the respective stop bands are centered around different frequencies. In the following, we refer to the mode above (below) the TM_{00} stop band as the ν_+ (ν_-) mode. In the square-notch configuration [Fig. 3(b)], the ν_+ and ν_- modes exhibit a rather large difference in the threshold gain, while in the configuration with tapered notches [Fig. 3(c)] both modes exhibit similar levels with values close to the FP case. In the square-notch configuration, the grating causes a stop band for the TM_{00} modes with a width of about 11 cm^{-1}, while for tapered notches the stop band width is somewhat reduced (8 cm^{-1}). In principle, modes with TM_{01} symmetry are also allowed in these systems. They might be excited if their threshold gain is smaller or similar to the one of close-by TM_{00} modes. According to Fig. 3(c), the tapered-notch configuration should provide a better suppression of TM_{01} modes. How can we distinguish between TM_{00} and TM_{01} modes experimentally? First, TM_{00} and TM_{01} modes have different far-field signatures – in contrast to the TM_{00} mode, the y-polarized component of the TM_{01} far field should exhibit a node at $\beta = 90°$. Second, the stop bands of TM_{00} and TM_{01} modes also shift differently with the grating period (not shown), which is due to the different dispersion relations. From two-dimensional waveguide simulations, we found that at 3 THz the effective index for the TM_{00} mode is about 3.05 for a 15 μm wide waveguide and about 1.08 for the TM_{01} mode. Hence, if excited, the TM_{01} modes might constitute a case of first-order grating emission.

#199359 - $15.00 USD Received 14 Oct 2013; revised 18 Dec 2013; accepted 18 Jan 2014; published 5 Feb 2014

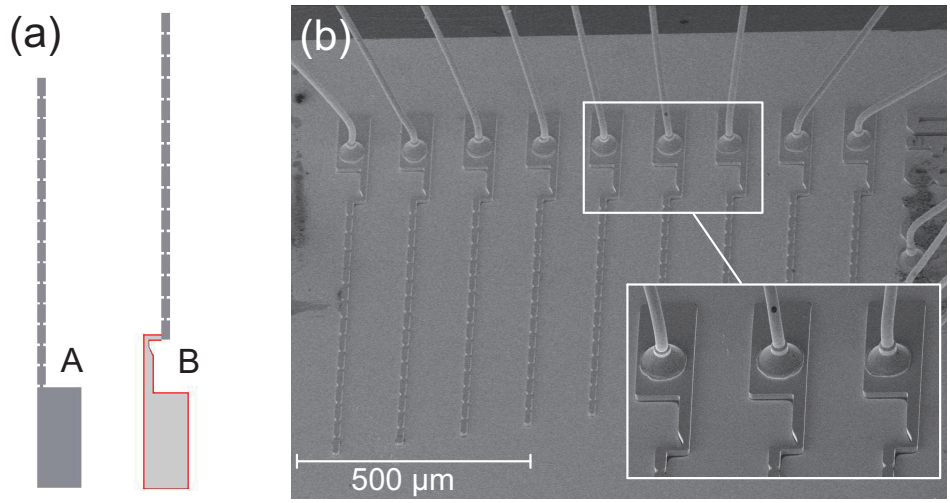

Fig. 4. (a) Top view of 3ODFB resonator designs with contact pads of type A and B. For type B, the light grey region depicts the contact pad area, which is insulated from the active region by a SiO_x layer (red) underneath. The actual 3ODFB ridges are 15 μm wide in the broad sections. (b) Scanning electron microscope image of a 3ODFB chip with type-B contact pads.

3. Experimental results and discussion

In this section, we present the experimental results for THz QCLs based on SP waveguides and narrow MM waveguides (with and without 3ODFB gratings), which are fabricated from the same wafer. The aim is to allow for a direct comparison of two application-relevant but very different waveguide/resonator concepts for THz QCLs without the effect of wafer-to-wafer variations. The active region of the investigated wafer is based on the GaAs/(Al,Ga)As heterostructure design for emission around 3 THz, which is described in [20]. It relies on phonon-assisted inter-miniband transitions and belongs to a class of interlaced bound-to-continuum/resonant-phonon designs. The active region with 85 periods has been grown on a semi-insulating GaAs substrate by molecular beam epitaxy. The layer sequence for one period is given by **3.8**/11.8/**0.5**/11.8/**1.0**/12.4/**1.9**/11.3/**2.9**/9.1/**2.9**/8.2/**2.9**/6.8/**2.9**/<u>16.3</u>/**2.9**/13.9, where the thickness is given in nm, bold numbers refer to the $Al_xGa_{1-x}As$ barriers ($x = 0.18$), and the underlined number denotes the Si-doped GaAs layer. The nominal doping density for that layer is 3×10^{16} cm^{-3}, while post-growth capacitance-voltage measurements yielded a value of 3.6×10^{16} cm^{-3}. In comparison to the resonant-phonon design used for achieving the currently highest pulsed operating temperatures [7], the applied active-region design allows for much smaller operating voltages and current densities and consequently a significantly reduced driving power density. This is a clear advantage for cw operation, since it helps to reduce the self-heating of the active region during cw operation as well as the total dissipated power, which has to be removed from the system. Since the threshold current (and hence the driving power) of THz QCLs is known to depend on the doping density [21, 22], the proper choice of the doping level is of course also important for a good cw performance.

Standard SP QCLs with 120 to 200 μm width were fabricated by wet etching and using AuGe top and bottom contacts. For the fabrication of MM QCLs, another part of the wafer

#199359 - $15.00 USD Received 14 Oct 2013; revised 18 Dec 2013; accepted 18 Jan 2014; published 5 Feb 2014

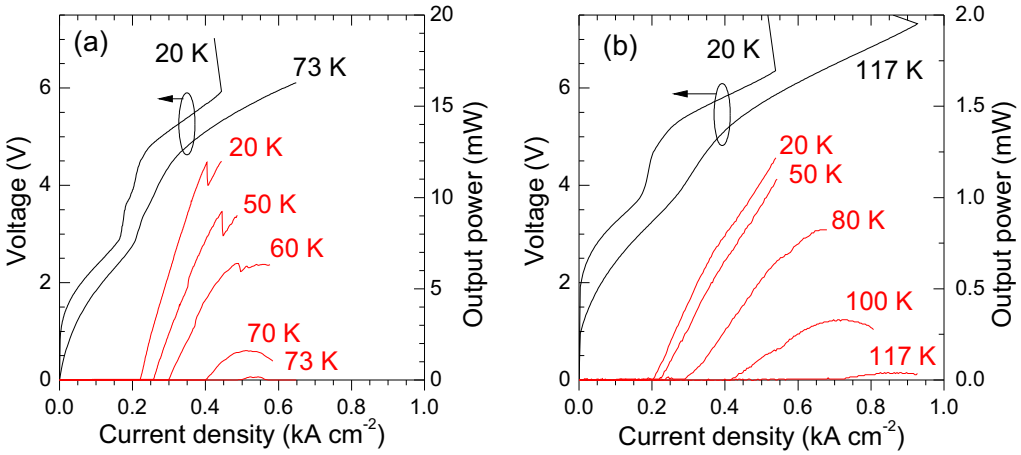

Fig. 5. (a) *L-J-V* performance (cw) of a 0.12×1.28 mm^2 SP QCL (FP resonator). The power has been corrected for a collection efficiency of 30%. (b) *L-J-V* performance (cw) of a 3ODFB QCL of type A with 15/5 μm width in the wide/narrow section and $\Lambda = 45$ μm (the total device area is 2.65×10^{-2} mm^2). The power has been corrected for a collection efficiency of 17%.

as well as a GaAs receptor substrate were covered with Ti/Au (10/500 nm) and subsequently bonded with each other by Au-Au thermo-compression wafer bonding. This was followed by a substrate removal step, in which the substrate of the epitaxial wafer is taken off by wafer lapping and selective wet etching.

Since contacting a 15 μm wide ridge directly by wire bonding is virtually impossible, the experimental situation deviates from the idealized resonators discussed above by the presence of contact pads. The two configurations shown in Fig. 4(a) have been investigated. For type A, a single lithographic mask is used to define the top-metal contact of the QCL ridge as well as the contact area for wire bonding. Subsequently, the top metallization (Ti/Au, 10/500 nm) is used as a self aligned mask for dry etching, which was performed in a reactive ion etching system based on an inductively coupled plasma (SAMCO RIE-140iP). The contact pads for wire bonding are directly attached to the laser ridge in this configuration. The resonator length was chosen in such a way that the total length is an integer multiple of the grating period. In configuration B, the contact pads are spatially separated from the laser ridge to provide an optical insulation from the intended resonator. A SiO_x passivation is applied in the region of the contact pads prior to the metallization step in order to avoid electrical pumping of the active region underneath. Figure 4(b) shows an image of a mounted 3ODFB chip of type B. To efficiently use the available material, each chip contains up to nine laser ridges. Caused by the applied mask writing setup, the edges in the realized structure are somewhat smoothed, resulting in tapered grating teeth, similar to the modeled situation in Fig. 3(c). After processing, laser chips were soldered with indium to oxygen-free copper submounts and subsequently contacted by wire bonding. Neither substrate thinning, nor facet coatings have been applied.

Figure 5(a) depicts the light-current density-voltage (*L-J-V*) characteristics of a 120 μm wide SP QCL under cw operation. At the lowest temperatures, a maximum output power of 12 mW is obtained, which decreases to 1.6 mW at a heat sink temperature of 70 K. Lasing was

#199359 - $15.00 USD Received 14 Oct 2013; revised 18 Dec 2013; accepted 18 Jan 2014; published 5 Feb 2014

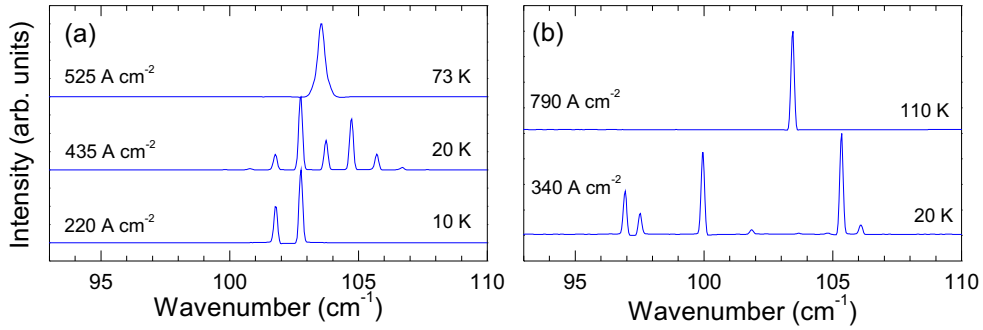

Fig. 6. (a) Emission spectra for the SP QCL of Fig. 5(a). (b) Emission spectra for the 3ODFB QCL of Fig. 5(b).

observed up to 73 K in cw mode. The threshold current density is 215 A cm^{-2} at the lowest operating temperatures, increasing to 500 A cm^{-2} at 73 K, with a total electrical driving power in the range of 1.5–5.3 W. The maximum slope efficiency at 20 K is about 58 mW/A. Although the performance data are shown for a FP laser, which usually emits in a multi-mode regime, we have demonstrated that similar single-mode cw output-power levels can be obtained for SP QCLs in combination with a lateral DFB grating of first order [23]. We attribute the slightly improved performance of the employed active region design with respect to our previously reported results [20] to a combination of improved growth conditions, such as in-situ growth rate control [24], and a slightly increased Al content in the barriers.

In Fig. 5(b), the *L-J-V* performance is shown for a 3ODFB QCL of type A. At the lowest temperatures, the threshold current density is almost the same as for the SP QCL. Since the device areas differ by a factor of 6, the value of the total threshold current is only about 1/6 of that for the SP QCL. The increase of the threshold current density with temperature is much smaller than for the SP QCL, which allows for cw operation up to 117 K with a total driving power in the range of only 0.25–1.8 W. The operating voltage for the 3ODFB QCL is somewhat larger than for the SP QCL, which is due to a Schottky contact at the bottom side, since no oxide removal step was performed prior to the Ti/Au deposition for wafer bonding. The maximum output power at 20 K is 1.2 mW, which is only 1/10 of the maximum power obtained for the SP QCL, and the maximum slope efficiency is only about 17 mW/A. Due to the better temperature performance, the situation changes above 70 K. At 80 K, still 0.8 mW of output power are obtained for the 3ODFB QCL, while the SP QCL already turned off.

The corresponding emission spectra for the SP and 3ODFB QCL (type A) are shown in Figs. 6(a) and 6(b), respectively. While the SP QCL exhibits a typical FP emission comb in the range of 101–106 cm^{-1}, the spectral signature of the 3ODFB QCL consists of several unequally spaced modes spanning the range of 97–106 cm^{-1}. Only close to their respective maximum operating temperature, both lasers become single mode, which is explained by a decrease of the gain toward higher temperatures allowing only for one mode close to the gain peak to reach the lasing threshold. We explain the broader emission range of the 3ODFB QCL at low temperatures by the broad gain spectrum of the active region in combination with a smaller threshold gain as compared to the SP QCL. Furthermore, we found that the complex emission pattern for the 3ODFB QCLs is related to the design of the contact pad (type A). Since the contact pad is part of the resonator, modes which are localized inside the contact pad area can easily couple to modes of the intentional 3ODFB stripe. A typical spectral feature for

#199359 - $15.00 USD Received 14 Oct 2013; revised 18 Dec 2013; accepted 18 Jan 2014; published 5 Feb 2014

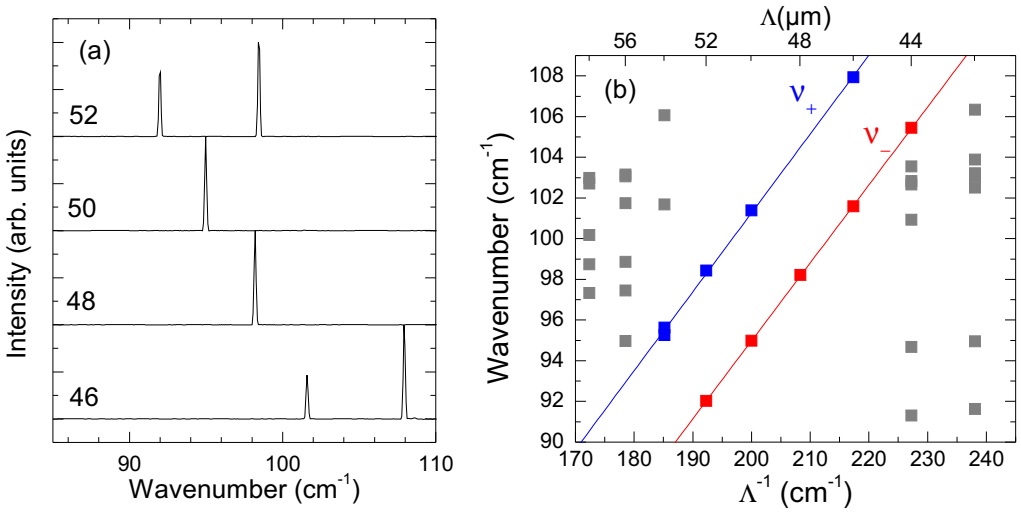

Fig. 7. (a) Emission spectra of 3ODFB QCLs of design type B, for grating periods in the range 46–52 μm. The lasers were operated in cw at 50 K close to their maximum output power. (b) Wavenumber of the different emission lines vs. inverse grating period for all nine lasers on the chip ($\Lambda = 42...58$ μm). Red (blue) symbols correspond to the identified ν_- (ν_+) modes and the lines to the respective linear fits.

such lasers is the appearance of pairs of modes with a rather small spacing [cf. Fig. 6(b)]. In an intuitive picture, this can be explained by the superposition of FP modes of a cavity with length l and a cavity with length $l - l_c$, where l_c denotes the length of the contact pad. Hence, longitudinal modes are reflected at both edges of the contact pad. A detailed investigation of the spectra and the corresponding complex beam profiles of type-A lasers is beyond the scope of this paper. For technical reasons related to the applied wire-bonding method, we could not reproduce the more compact contact pad design of Amanti et al. [9]. However, in case of the presented type-A lasers, the evidence for an impact of the contact pads on the mode spectrum is rather striking.

We continue with the discussion of MM wire QCLs of design type B. For this type, the contact pad is spatially separated from the intended resonator. The electrical connection is provided by a thin bridge [cf. Fig. 4(a)], which minimizes the optical coupling between the contact pad and 3ODFB stripe. In Fig. 7(a), lasing spectra are shown for grating periods in the range 46–52 μm. In this range, the spectra contain only one or two lasing modes, which can be identified as the ν_- or ν_+ stop band mode of the 3ODFB resonator. The corresponding stop band width is about 6.3 cm^{-1}, which fits well with the calculated TM_{00} stop band width for tapered grating notches (about 8 cm^{-1}). Single-mode operation with a strong side-mode suppression ratio of 30 dB was only observed for the grating period of 48 μm. For grating periods outside the range of 46–52 μm, the spectra contain typically several additional modes. In Fig. 7(b), the wavelengths of the emission lines are plotted for grating periods of 42–58 μm, corresponding to the nine lasers on one chip. In the presence of both stop band modes, it is possible to determine the Bragg frequency via $\nu_B = (\nu_+ + \nu_-)/2$. The slope of $\lambda_B(\Lambda)$ and $\nu_B(\Lambda^{-1})$ then contains

#199359 - $15.00 USD Received 14 Oct 2013; revised 18 Dec 2013; accepted 18 Jan 2014; published 5 Feb 2014

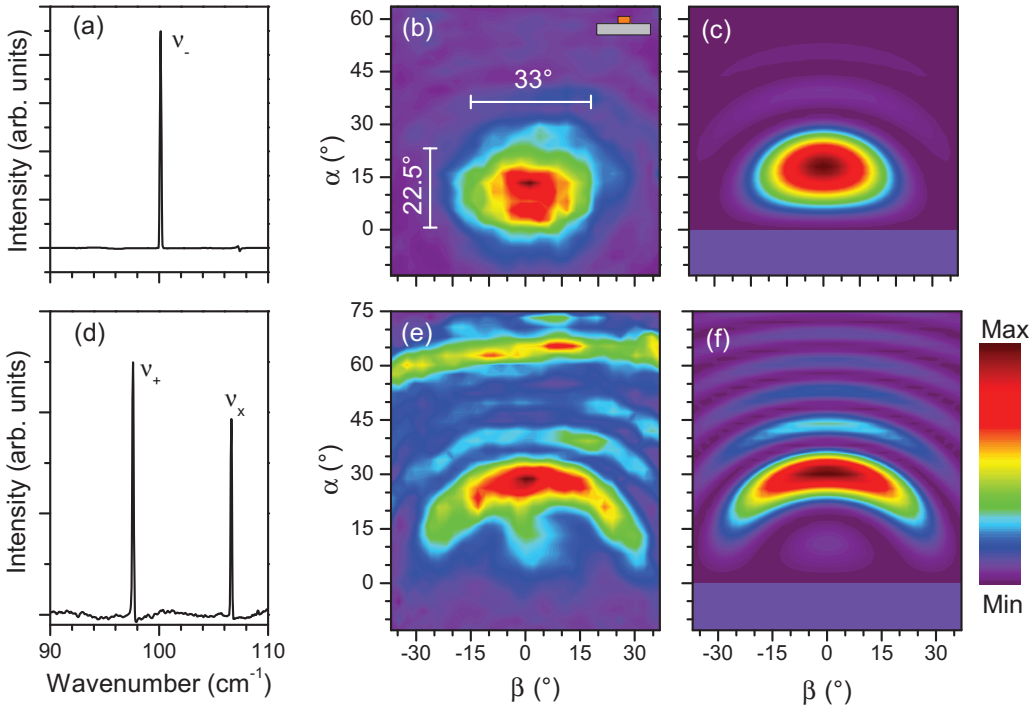

Fig. 8. (a) Measured spectrum for a 3ODFB QCL of design type B with $\Lambda = 48$ μm emitting in the ν_- mode. (b) Measured far field corresponding to (a). (c) Calculated far field corresponding to (a) with $r = 44$ ($s = -1$, $n_r = 3.05$). (d) Emission spectrum for a 3ODFB QCL with $\Lambda = 54$ μm. (e) Measured far field corresponding to (d). (f) Calculated far field corresponding to the ν_+ mode in (d) with $r = 45$ ($s = 1$, $n_r = 2.85$). For (a), (b), (d), and (e), the lasers were operated at 50 K in pulsed mode (10 μs pulses, 20% duty cycle).

information about the effective index $n_e(\Lambda)$ and its linear dispersion

$$\frac{d\lambda_B}{d\Lambda} = \frac{2}{M}\left(n_e + \frac{dn_e}{d\Lambda}\Lambda\right), \tag{9}$$

$$\frac{d\nu_B}{d\Lambda^{-1}} = \frac{M}{2n_e^2}\left(n_e + \frac{dn_e}{d\Lambda}\Lambda\right). \tag{10}$$

For a given grating order M, these are two equations for the two unknown variables n_e and $dn_e/d\Lambda$. With $M = 3$, we find $n_e(\Lambda) = 3.07 - 0.014(\Lambda[\mu\text{m}] - 49)$ from the measured peak positions. Note that n_e differs in general from the resonator refractive mode index n_r as used for the antenna model. To determine n_r, we need the number of maxima inside the resonator for the ν_+ and ν_- modes. The number of maxima is approximately $r_\pm = 2Ln_e\nu_B \pm 0.5$. The integer value which is closest to the numerical value is 44 (45) for the ν_- (ν_+) stop band mode. The resonator mode index is then simply given by $n_{r,\pm} = r_\pm/(2L\nu_\pm)$. Since even (odd) numbers correspond to antisymmetric (symmetric) modes, all parameters for the antenna model are fixed and allow for a comparison of the measured and calculated far fields.

Figures 8(a) and 8(b) depict the measured emission spectrum and the corresponding beam profile for a 3ODFB QCL of design type B with $\Lambda = 48$ μm, respectively. The laser exhibits a rather narrow emission cone with a full width at half maximum (FWHM) of 22.5° and 33° in the

#199359 - $15.00 USD Received 14 Oct 2013; revised 18 Dec 2013; accepted 18 Jan 2014; published 5 Feb 2014

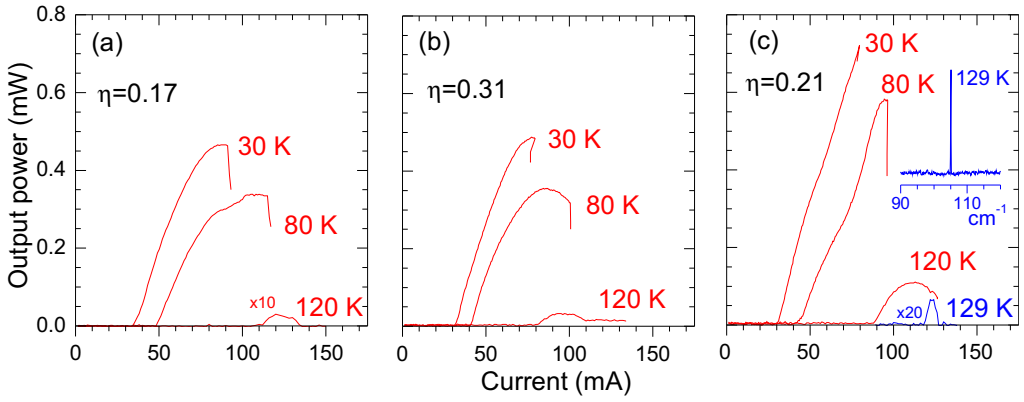

Fig. 9. Measured cw output power vs. current for three different MM wire QCLs with contact pads of type B (η: collection efficiency). (a) 15 μm wide and 675 μm long FP QCL (resonator area 1.01×10^{-2} mm^2), (b) 3ODFB QCL with $\Lambda = 48$ μm (resonator area 0.97×10^{-2} mm^2), and (c) 3ODFB QCL with $\Lambda = 44$ μm (resonator area 0.87×10^{-2} mm^2). The inset in (c) depicts the cw emission spectrum taken at 129 K.

vertical and lateral direction, respectively. According to Fig. 7(b), we can ascribe the emission line to the ν_- mode. Figure 8(c) depicts the calculated far field according to the antenna model for $r = 44$. There is a rather good agreement between the measured and calculated far field with one main difference. Due to the assumption of an infinite metal plane underneath the resonator, the far-field intensity for $\alpha \leq 0$ must be equal to zero in the antenna model. In contrast, the intensity for the measured far field does not vanish at $\alpha = 0$. The effect, which improves the shape toward a more circular beam, is hence related to the finite size of the mounted laser chip. Figures 8(d)–8(f) depict the situation for a 3ODFB QCL of design type B with $\Lambda = 54$ μm, which emits in the ν_+ mode and an additional mode ν_x. There is again a clear correlation between the measured and calculated beam profile ($r = 45$). The measured intensity maximum around $\alpha = 60°$ can be attributed to the ν_x mode in the spectrum, which is not taken into account in the simulations.

We found that there is a discrepancy between the finite-element calculations shown in Fig. 3 and the parameters for the antenna model obtained from the experiments. According to the simulations, the ν_- (ν_+) mode should correspond to $r = 45$ (46) as compared to $r = 44$ (45) obtained from the experimental data. We attribute this discrepancy to the idealized boundary conditions, which are assumed for the antenna model. In reality, the intensity does not vanish at the resonator ends due to the finite facet reflectivity.

Finally, we will discuss the output power performance of lasers with contact pads of type B. Figure 9(a) depicts the light-current (*L-I*) characteristics for a multi-mode FP resonator, Fig. 9(b) for a single-mode 3ODFB QCL ($\Lambda = 48$ μm), and Fig. 9(c) for another 3ODFB QCL ($\Lambda = 44$ μm) emitting in a multi-mode regime at low temperatures. The *L-I* performances of FP and 3ODFB QCLs are surprisingly similar, having almost the same threshold current density, comparable levels of output power, and comparable operating temperature ranges. All lasers operate in cw mode at a temperature of 120 K, with a maximum operating temperature of 129 K in case of the 3ODFB QCL with $\Lambda = 44$ μm [cf. Fig. 9(c)]. For comparison, the same device operated in pulsed mode up to 149 K (1 μs pulses, 10% duty cycle). Apparently, there is not much difference in the output power of the 15 μm wide FP QCL and the 3ODFB QCLs.

#199359 - $15.00 USD Received 14 Oct 2013; revised 18 Dec 2013; accepted 18 Jan 2014; published 5 Feb 2014

This is consistent with simulation results shown in Fig. 3, which predict similar radiation losses for both resonator types. However, the collection efficiency is increased in case of the 3ODFB gratings due to the better beam profile. Note that due to geometric restrictions set by the cryo-cooler the output power can only be measured within a limited solid angle. The output power in Figs. 9(a)–9(c) equals the total power emitted within a cone of 66° (full opening angle). Since the output power of the FP QCL lies in the range of values for the 3ODFB QCLs, we conclude that the applied 3ODFB grating improves the shape of the beam profile, but does not result in significantly larger radiation losses. Of course, the spectral radiance, i.e. the intensity per steradian and frequency interval, is much larger in case of single-mode 3ODFB QCLs. We believe that the superior high-temperature performance of the 3ODFB QCL with $\Lambda = 44\ \mu$m is due to a favorable combination of a low-threshold resonator mode (close to the gain maximum for the particular high-temperature driving conditions) with an optimum resonator size (depending on the grating period in our configuration).

In Fig. 9, we refer to the absolute driving current. Dividing it by the area of the actual resonators (cf. caption of Fig. 9), we find an increased threshold current density as compared to lasers of design type A. Since the current density for the onset of voltage instabilities is also shifted (not shown), we explain the discrepancy by a parasitic current flow underneath the SiO_x passivated contact pads. Actually, we found that due to a small alignment offset during processing the SiO_x passivation did not cover the full area of the contact pads. By comparing the current-voltage characteristics of samples of type A and B, we estimate that the parasitic current in MM wire QCLs of type B accounts for about 40% of the total current.

The slope efficiencies range between 12 mW/A for the FP QCL in Fig. 9(a) and 17 mW/A for the 3ODFB QCL in Fig. 9(c). If we correct for the parasitic currents, the values increase to 20 and 28 mW/A, respectively. However, this is still well below the 58 mW/A of the SP QCL and also much lower than the value of 150 mW/A reported by Amanti et al. [9]. According to the common laser theory, the slope efficiency is proportional to the ratio of the radiation losses to the total losses $\alpha_r/(\alpha_r + \alpha_i)$ [25]. From the finite-element simulations, we expect this ratio to be in the range 0.3–0.4 for the investigated 3ODFB QCLs and about 0.6 for the SP QCL (assuming $\alpha_r = 10\ \mathrm{cm}^{-1}$ for the mirror losses and $\alpha_i = 6\ \mathrm{cm}^{-1}$ for the internal losses). Hence, the experimental results are consistent with the simulations. A larger slope efficiency should be obtained in case of lasing in the TM_{01} modes, since the corresponding radiation losses can be much larger than for the TM_{00} modes.

The remarkable temperature performance of the MM wire QCLs (with and without 3ODFB grating) points toward two aspects. On the one hand, MM waveguides are known to allow for operation at higher temperatures than SP QCLs due to a better mode confinement. On the other hand, for MM wire QCLs the narrow ridge width helps to increase the cw operating temperature. As an example, for 50 μm wide MM QCLs, we observed cw operation only up to 95 K. Hence, we can confirm the result of Amanti et al. [9] of a superior temperature performance for MM wire QCLs. Apparently, a smaller total thermal load is a big advantage for cw operation. In terms of thermal management, an important measure is the self-heating of the device during cw operation. It is reflected by the difference between the maximum pulsed and cw operating temperature, which is as small as 20 K in our case, while values as small as 10 K have already been reported for MM wire QCLs based on a similar active-region concept [9, 22]. The key for these results appears to be a combination of both, the small size of MM wire resonators, resulting in a small total thermal load, which has to be removed from the system, along with an active-region design requiring low driving power densities. Further systematic studies on the thermal management of MM wire QCLs might help to clarify this issue. Indeed, we believe that the thermal performance is limited by the heat conductance across interfaces such as the solder interface between the chip and submount and not so much by the bulk thermal conductivity

#199359 - $15.00 USD Received 14 Oct 2013; revised 18 Dec 2013; accepted 18 Jan 2014; published 5 Feb 2014

of the involved materials, which is typically much larger at the operating temperatures of THz QCLs as compared to room temperature.

4. Summary and conclusions

Based on the same wafer, we investigated the performance of THz QCLs with SP and MM waveguides, where in the latter case the focus has been on MM wire QCLs for which the ridge width is small compared to the emission wavelength. While SP QCLs are superior in terms of maximum output power and slope efficiency, MM wire QCLs allow for cw operation up to much higher temperatures. While the maximum cw operating temperature of a SP QCL was 73 K, a MM wire QCL from the same wafer operated up to 129 K. For comparison, the previously reported highest cw operating temperature for a THz QCLs has been 117 K [6]. We found that the total spectral coverage is in general larger for QCLs based on MM waveguides, which we attribute to a smaller threshold gain for MM QCLs in combination with a broad gain spectrum of the active region. Due to spatial hole burning, this can cause a poor side-mode suppression ratio or even strong multi-mode operation in case of MM wire QCLs with a 3ODFB resonator. Hence, we conclude that broad-band active regions are not well suited for single-mode operation over a larger spectral range. We found that the design of the contact pads can have a rather large impact on the characteristics of 3ODFB QCLs. Predictable single-mode operation with a narrow beam profile was obtained for contact pads, which are optically insulated from the intended 3ODFB resonator. In terms of total output power and slope efficiency, we did not observe a clear difference between MM wire QCLs with FP and 3ODFB resonators. However, by improving the shape of the beam profile and allowing for single-mode operation, the spectral radiance of 3ODFB resonators can become significantly enhanced as compared to pure FP resonators. A good agreement was obtained between measured beam profiles and calculations based on an antenna model, showing a clear interdependence of the emission spectra and the beam profile. We found that for a particular resonator geometry the beam profile is solely determined by the emission wavelength and the number of intensity maxima inside the resonator.

Acknowledgments

The authors would like to thank M. Höricke and W. Anders for accompanying sample growth and processing, respectively, L. Zschiedrich and S. Burger from JCMwave for technical support, and X. Lü for a careful reading of the manuscript. This work was supported in part by the Investitionsbank Berlin (grant no. 10146490) within the EFRE program of the European Union.

#199359 - $15.00 USD Received 14 Oct 2013; revised 18 Dec 2013; accepted 18 Jan 2014; published 5 Feb 2014